

dependently of the calculations by Andersen *et al.*¹¹ The transitions between T and OI phases and between OI and OII were calculated by the cluster variation method (CVM) to be of second kind (full curves),⁵ but the originally calculated OII curve is here displaced downwards by about 50 K to show a small temperature gap between the two transition lines, in accordance with more recent experimental results.¹² Another phase region, that of the OIII (or $\langle 110 \rangle$) phase (dashed lines), was also calculated by the CVM.¹³ The pronounced asymmetry towards higher oxygen concentrations was already suggested by a graph of the HPU hierarchy applied to the YBCO model.⁶ The other long-period phases are shown as arising by first-order peritectoid reactions, but the actual location of the phase boundaries (dashed curves), in concentration and temperature, has not been calculated and is conjectured based on the known hierarchy of the phases, and on the high-oxygen asymmetry mentioned in conjunction with the $\langle 110 \rangle$ phase. According to the HPU algorithm, the structure formula of each lower-temperature phase is obtained by telescoping the formulas of the two higher-temperature phases giving rise to it. Successively longer-period phases occur at decreasing temperature and require increasingly longer-range interactions for their thermodynamic stability. Accordingly, as an $x=6.63$ sample (dashed vertical line in Fig. 1), of interest here, is cooled from a high temperature in the OI orthorhombic phase, it successively passes through (or close to) the $\langle 110 \rangle$, $\langle 11010 \rangle$ and $\langle (110)^2 10 \rangle$ phase regions.

The two-dimensional Ising model approach to low-temperature phase transformations in YBCO is a convenient one to investigate oxygen ordering in this compound. To that effect, we performed Monte Carlo (MC) simulation runs on an 80×80 square lattice at constant concentration of $c=0.315$ (corresponding to oxygen content of $x=6.63$ in the actual compound).¹⁴ Oxygen configurations were randomized at 1400 K, then “aged” at various lower temperatures by performing typically several thousand MC steps per site. Final occupation patterns displayed alignments of O sites preferentially along one of the square directions, confirming the expected tendency to form long (but not perfect) chains. Fourier transforms of the resulting patterns were taken and resulting intensities were plotted along the direction normal to the chains.

In a typical run, the intensity spectrum at 700 K gives clear evidence of short-range order (SRO) at wave vector $h=0.5$. This result is expected because, in the OI region at $x=6.63$, the SRO wave vector should be that of the concentration wave responsible for the second-order transition into the lower-temperature phase, the OII phase ($\langle 10 \rangle$). At 500 K the situation is less clear: the peak is still present at the same location, as expected in the OI region, but it is broadened probably due to imperfect $\langle 10 \rangle$ ordering. The situation at 300 K can best be described as one characteristic of a mixture of ordered phases: there are diffuse peaks around wave numbers roughly indicative of the OIII and OII phases, in good qualitative agreement with the expected phase diagram. At 200 K of the MC simulation the one-dimensional structure peaks are well formed, having maxima at wave numbers $h=\frac{3}{8}$ and $\frac{5}{8}$, which are the correct wave vectors for the strongest Fourier components of the $\langle (110)^2 10 \rangle$ structure, whose

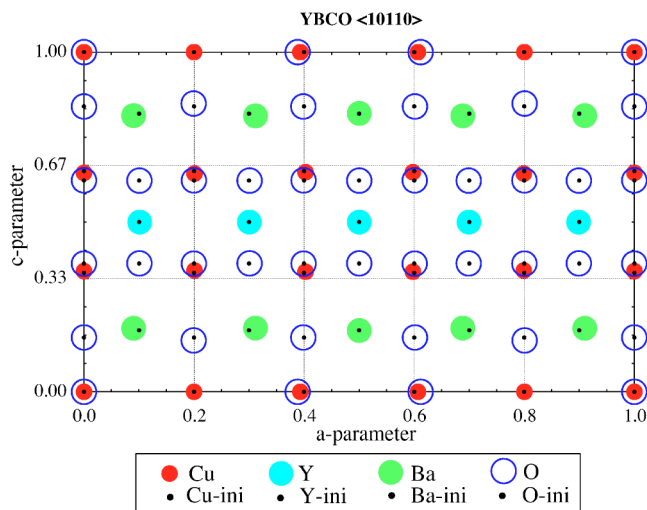


FIG. 2. (Color online) The projected unit cell along the \mathbf{b} direction of the unit cell of the $\langle 10110 \rangle$ structure showing atomic displacements (amplified by a factor of 4 for better visibility) from fully relaxed LDA *ab initio* electronic structure calculations.

stoichiometric composition is precisely that of the 6.63 sample investigated experimentally.³

The MC simulations suggest that oxygen ordering in the $x=6.63$ YBCO superconductor can be expected to take place, producing $\langle 11010 \rangle$ (OrthoV) and/or $\langle (110)^2 10 \rangle$ structures at low temperatures, with wave vectors in the vicinity of $h=\frac{2}{5}$ (and $\frac{3}{5}$) and of $h=\frac{3}{8}$ (and $\frac{5}{8}$), respectively. In x-ray diffraction studies by Islam and co-workers,³ the observed superlattice peaks, reproduced here in Fig. 3 (to be described below), are centered on $h \sim \frac{2}{5}$ and (and $\sim \frac{3}{5}$) expected for the OrthoV structure. Due to imperfect short-range ordering of these phases, however, the peaks are rather diffuse and, within experimental errors, are consistent with the strongest Fourier components, $h=\frac{3}{8}$ and $\frac{5}{8}$, of the ideal $\langle (110)^2 10 \rangle$ structure whose stoichiometric composition is precisely $x=6.63$. In what follows, we provide direct proof that atomic displacements driven by oxygen ordering in the CuO planes are responsible for these satellites. For that purpose, we calculate the structure factors of perfectly ordered stoichiometric $\langle 11010 \rangle$ and $\langle (110)^2 10 \rangle$ long-period structures at absolute zero, *static* atomic displacements being obtained from “first principles,” i.e., by *ab initio* electronic structure computations with relaxed atomic positions within the unit cell.

A 63-atom orthorhombic cell representing the fully ordered $\langle 11010 \rangle$ structure was constructed by repeating five unit cells of the $\text{YBa}_2\text{Cu}_3\text{O}_7$ cell along the \mathbf{a} direction with O atoms removed in two chains along the \mathbf{b} direction in the Cu—O plane. The unit cell of the perfect $\langle 10110 \rangle$ structure is shown in Fig. 2 projected along the \mathbf{b} direction. Large filled circles represent Ba atoms (nominally at positions $z=0.25$ and 0.75 , green in the color version), medium-sized filled circles represent Y atoms (at $z=\frac{1}{2}$, brown), small filled circles represent Cu atoms (at $z=0, \frac{1}{3}, \frac{2}{3},$ and 1 ; red) and O atoms are represented by large open circles (blue). Small filled circles indicate starting ideal positions of all atoms. The atomic relaxation calculations proceeded as follows: All

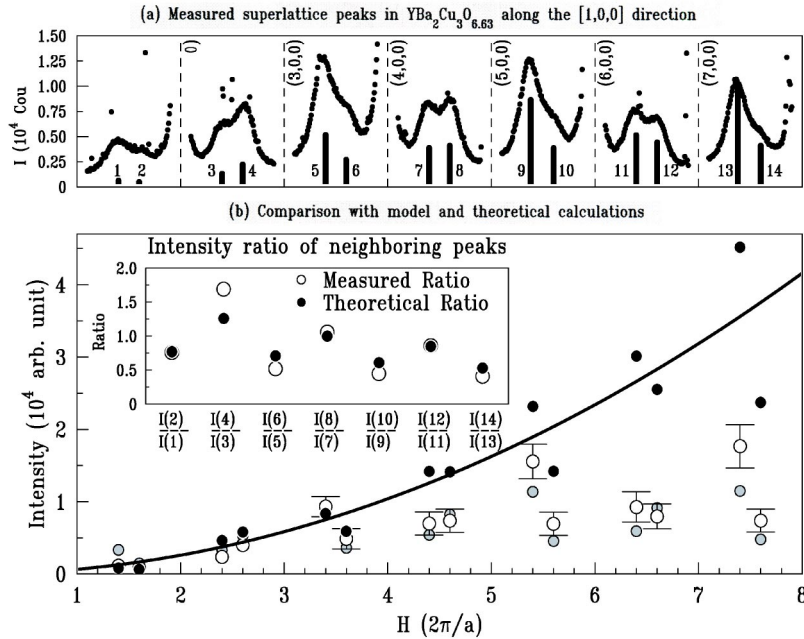


FIG. 3. (Color online) The comparison of intensities for peaks observed in $[H 0 0]$ -scans: (a) high-energy x-ray diffraction measurements from an underdoped YBCO sample at 14 K (main Bragg points indicated by dashed lines); vertical red lines indicate integrated intensity; (b) calculated structure factors along the same direction for OrthoV ($\langle 10110 \rangle$) structure; red circles: observed intensity; blue circles: theoretical structure factors without including Debye-Waller factors; black circles: structure factor using approximate F^2 expression; blue line: Q^2 behavior; inset: measured and theoretical intensity ratios for immediate-neighbor satellites as indicated by the ratio of satellite intensities at $h = \frac{3}{5}$ to $h = \frac{2}{5}$.

ions were relaxed to positions of static equilibrium using quantum-mechanical Hellman-Feynman forces, which were calculated using the *ab initio* VASP code.¹⁵ Coulomb interactions between electrons and ions were represented by ultrasoft Vanderbilt-type pseudopotentials¹⁶ as supplied by Kresse and Hafner.¹⁷ Electronic wave functions were expanded in plane waves with a cutoff energy $E_{\text{cut}} = 494$ eV. Exchange and correlation effects were treated within the local-density approximation (LDA). Electronic states were summed over a regular $2 \times 8 \times 2$ k -point grid and broadened with a first-order Methfessel-Paxton function of width 0.15 eV. In Fig. 2, calculated atomic displacements have been scaled up by a factor of 5 to make them more visible. For the most part, the displacements are in the expected directions: Y, occupying highly symmetric positions, are hardly displaced, the rumpled Cu—O₂ planes tend to flatten out, and O atoms move towards the empty chains, laterally in the Cu—O planes and vertically by fairly large amounts for the apical oxygens. Characteristically, the very large displacements of the Ba atoms are *away* from empty O sites. Calculations for the $\langle (110)^2 10 \rangle$ unit cell gave similar results (not shown).

The critical test is now to see whether the calculated structure factor from the relaxed unit cell (Fig. 2) reproduces in its essential features the experimental diffraction patterns obtained by Islam *et al.*³ Since x-ray diffraction intensity at a given diffraction vector \mathbf{Q} is essentially proportional to the square of the Fourier transform (structure factor) of electronic density for the corresponding \mathbf{k} vector, structure factors were calculated directly from Fourier transforming the total electronic charge density:

$$\rho(\mathbf{k}) = \sum_{j=1}^{N_{\text{at}}} Z_j^{\text{core}} e^{i\mathbf{k} \cdot (\mathbf{R}_j + \mathbf{u}_j)} + \int \rho_v(\mathbf{r}) e^{i\mathbf{k} \cdot \mathbf{r}} d\mathbf{r} \quad (1)$$

where R_j is the crystallographic position of ion j in the ideal unit cell (small filled circles in Fig. 2), \mathbf{u}_j is its displacement to the equilibrium (relaxed) position (large open circles Fig.

3), Z_j^{core} is the number of core electrons, and $\rho_v(\mathbf{r})$ is the valence charge density, which was obtained from *ab initio* electron-structure calculations on supercells with O vacancies, as described above. Since we are using a periodic supercell, the calculated structure factor is nonzero only at wave vectors that are multiples of the reciprocal lattice vectors of the supercell.

We may now compare calculated diffraction patterns with those from experiments. The upper panel (a) of Fig. 3 displays the x-ray diffraction profiles (black dots) along the $[1,0,0]$ direction of the reciprocal lattice, taken at 14 K from a high-quality, well-annealed crystal of $\text{YBa}_2\text{Cu}_3\text{O}_{6.63}$. The data were taken on the 4ID-D beamline at the Advanced Photon Source of the Argonne National Laboratory, using 36 keV x rays (see Ref. 3). Broad overlapping satellite peaks, which are characterized by a single oxygen concentration wave at $h \approx \frac{2}{5}$ and $\frac{3}{5}$, are visible in between the Bragg points (integer values of H). Note the systematic behavior of the diffuse intensity: to the left (low angles) of the even-order main peaks satellites have a “dromedary-like” appearance (one hump), while to the right they have “camel-like” appearance (two humps). These diffuse peaks were fitted with a pair of Gaussian lines along with Lorentzian tails and a constant term accounting for thermal diffuse scattering and background, respectively. The intensity of the Gaussians representing the peaks was then corrected for geometric factors to obtain the integrated intensities shown in Fig. 3(a) by heavy vertical lines (red) located at satellite positions $\frac{2}{5}$ and $\frac{3}{5}$, their heights being proportional to the satellite intensities, about 10^6 times weaker than those of the Bragg peaks (indicated only as dashed lines). The corrected satellite intensities are also plotted as (red) circles with associated error bars on panel (b) of the same figure. Also shown on this panel are the squares of the structure factors (blue circles) of the relaxed OrthoV unit cell calculated *ab initio* from the total electron density as explained above.

The most striking feature of this comparison is the agree-

ment of alternating “dromedary” and “camel” features reproduced in both measured and calculated satellite intensities. This comparison is further illustrated by plotting, in the inset of Fig. 3, the ratio of intensities of neighboring satellites: the agreement is as close as can be expected, especially given the fact that the theoretical intensities were calculated from “first principles,” i.e., without a single experimental or adjustable parameter being used. Note that at higher values of H , calculated intensities continue to increase as the magnitude squared of the scattering vector (the curve Q^2 in the figure), whereas the actual intensities level off after about $H=5$. The discrepancy is due to the neglect in the theoretical calculations of the effect of static and dynamic displacive disorder. The point can be demonstrated as follows. Consider the standard formula for scattered amplitude $F(\mathbf{Q})$ (see Ref. 3, for example) in which the exponential involving the atomic displacements has been replaced by the linear term of its expansion, valid away from the fundamental reflections and for $|\mathbf{Q}\cdot\mathbf{u}|$ not too large:

$$|F(\mathbf{Q})|^2 = \left| \sum_j (\mathbf{Q}\cdot\mathbf{u}_j) f_j(Q) e^{-W_j(Q)} e^{-i\mathbf{Q}\cdot\mathbf{R}_j} \right|^2. \quad (2)$$

In this expression, the summation is over the index j of the atoms in the supercell, f_j are scattering form factors, and e^{-W_j} are experimentally determined Debye-Waller factors.¹⁸ Values of F^2 calculated for the satellites according to this formula are plotted as (black) open circles in Fig. 3(b), the values of the *static* atomic relaxations \mathbf{u} being taken from the *ab initio* calculations displayed in Fig. 2. The theoretical intensities, thus corrected approximately for displacive disorder, now agree quite well with the corrected experimental values (red). The approximate formula for the structure factor given here, but without the e^{-W} correction, also explains the Q^2 dependence of the theoretical intensities, calculated at 0 K.

To conclude: it should be evident from the foregoing that the periodic diffuse intensity modulations observed experi-

mentally in underdoped YBCO are caused by the ordering of oxygen in Cu—O planes, leading to predicted, well-defined one-dimensional “O-compositional stripes,” according to the phase diagram of Fig. 1. Of course, as the oxygen ions and the charged vacancies order, a corresponding charge density wave (CDW) is generated as well. The point is, however, that it is the atomic ordering that creates the charge density wave, not vice versa. As for the origin of the oxygen modulation, it is explained by electronic structure calculations and by the (exact) HPU algorithm as having been the diffraction effects due to atomic displacements resulting from relaxations around missing oxygen ions within the chains in oxygen-depleted phases. The calculation of the displacements shown in Fig. 2 was communicated to Islam *et al.*¹⁹ before they undertook the analysis of their diffraction data on optimally doped YBCO. Although there are some quantitative and qualitative differences between the data in underdoped and optimally doped materials, in the latter case, they found that the experimentally deduced correlated atomic displacements portray a pattern remarkably similar to that in Fig. 2. The conclusion reached in Ref. 19 that an O-ordered OrthoIV phase is responsible for the x-ray diffuse peaks is based on the first-principles calculations presented in this paper. The present calculation pertaining to underdoped YBCO shows that the experimentally obtained and calculated intensities based on theoretically deduced atomic displacements agree remarkably well, provided that an approximate Debye-Waller correction be applied, as shown.

Early work on oxygen ordering performed at UC Berkeley was funded by the Director, Office of Basic Energy Sciences (BES), Materials Science Division of the Department of Energy. The Advanced Photon Source is supported by DOE BES (Contract No. W-31-109-ENG-38). S.C.M. and V.O. acknowledge the support of the National Science Foundation through Grant Nos. DMR-0099573 and DMR-0427638, respectively.

¹T. Timusk and B. Statt, Rep. Prog. Phys. **62**, 61 (1999); J. L. Tallon and J. W. Loram, Physica C **349**, 53 (2001).
²J. Zaanen and O. Gunnarsson, Phys. Rev. B **40**, R7391 (1989); K. Machida, Physica C **158**, 192 (1989); S. A. Kivelson *et al.*, Nature (London) **393**, 500 (1998); B. Batlogg and C. M. Varma, Phys. World **13**(2), 33 (2000); Y. N. Ovchinnikov, S. A. Wolf, and V. Z. Kresin, Phys. Rev. B **63**, 064524 (2001).
³Z. Islam, S. K. Sinha, D. Haskel, J. C. Lang, G. Srajer, B. W. Veal, D. R. Haefner, and H. A. Mook, Phys. Rev. B **66**, 092501 (2002).
⁴D. de Fontaine, L. T. Wille, and S. C. Moss, Phys. Rev. B **36**, R5709 (1987); L. T. Wille and D. de Fontaine, *ibid.* **37**, 2227 (1988).
⁵G. Ceder, M. Asta, W. C. Carter, M. Kraitchman, D. de Fontaine, M. E. Mann, and M. Sluiter, Phys. Rev. B **41**, 8698 (1990).
⁶D. de Fontaine *et al.*, Nature (London) **343**, 544 (1990).
⁷G. Van Tendeloo *et al.*, Solid State Commun. **63**, 603 (1987).

⁸R. Beyers *et al.*, Nature (London) **340**, 619 (1989).
⁹J. Hubbard, Phys. Rev. B **17**, 494 (1978); V. L. Pokrovsky and G. V. Uimin, J. Phys. C **11**, 3535 (1978).
¹⁰P. Sterne and L. T. Wille, Physica C **162**, 223 (1989).
¹¹N. H. Andersen *et al.*, J. Less-Common Met. **164-165**, 124 (1990).
¹²M. von Zimmermann *et al.*, Phys. Rev. B **68**, 104515 (2003).
¹³G. Ceder *et al.*, Physica C **177**, 106 (1991).
¹⁴D. de Fontaine, V. Ozolins, and N. Speed, unpublished work at U. C. Berkeley.
¹⁵G. Kresse and J. Hafner, Phys. Rev. B **47**, R558 (1993); G. Kresse and J. Furthmüller, *ibid.* **54**, 11169 (1996).
¹⁶D. Vanderbilt, Phys. Rev. B **41**, R7892 (1990).
¹⁷G. Kresse and J. Hafner, J. Phys.: Condens. Matter **6**, 8245 (1994).
¹⁸R. P. Sharma *et al.*, Physica C **174**, 409 (1991).
¹⁹Z. Islam *et al.*, Phys. Rev. Lett. **93**, 157008 (2004).